ADVANCED ENERGY MATERIALS
www.advenergymat.de

Tailored p-Orbital Delocalization by Diatomic Pt-Ce Induced Interlayer Spacing Engineering for Highly-Efficient Ammonia Electrosynthesis

*Dong Chen, Shaoce Zhang, Di Yin, Wanpeng Li, Xiuming Bu, Quan Quan, Zhengxun Lai, Wei Wang, You Meng, Chuntai Liu, SenPo Yip, Fu-Rong Chen, Chunyi Zhi, and Johnny C. Ho**

Electrochemical nitrate reduction to ammonia (eNO_3RR) is a green and appealing method for ammonia synthesis, but is hindered by the multistep chemical reaction and competitive hydrogen generation. Herein, the synthesis of 2D SnS nanosheets with tailored interlayer spacing is reported, including both expansion and compression, through the active diatomic Pt-Ce pairs. Taking together the experimental results, in situ Raman spectra, and DFT calculations, it is found that the compressed interlayer spacing can tune the electron density of localized p-orbital in Sn into its delocalized states, thus enhancing the chemical affinity towards NO_3^- and NO_2^- but inhibiting hydrogen generation simultaneously. This phenomenon significantly facilitates the rate-determining step ($*NO_3 \rightarrow *NO_2$) in eNO_3RR, and realizes an excellent Faradaic efficiency (94.12%) and yield rate (0.3056 mmol cm^{-2} h^{-1}) for NH_3 at −0.5 V versus RHE. This work provides a powerful strategy for tailoring flexible interlayer spacing of 2D materials and opens a new avenue for constructing high-performance catalysts for ammonia synthesis.

1. Introduction

Ammonia (NH_3) is a newly developed green energy that can be used to produce fertilizers, chemicals, and carbon-free fuels.[1] Currently, the ammonia synthesis methods of the traditional Haber-Bosch process and electrochemical nitrogen reduction reaction (eNRR) have limited application conditions, such as harsh operating requirements and highly stable nonpolar N≡N bonds with high dissociation energy (945 kJ mol^{-1}).[2–5] Consequently, the electrochemical nitrate reduction reaction (eNO_3RR) to convert nitrate into ammonia is generally a more efficient synthesis scheme. It is considered one of the best pathways to an ammonia economy.[6,7] Compared with the Haber-Bosch process and eNRR, eNO_3RR is nonpolluting, has high efficiency under mild conditions, and the nitrate anion (NO_3^-) exhibits low dissociation energy of the N=O bond (204 kJ mol^{-1}).[8] More importantly, besides the redundant nitrates in agricultural and industrial wastewater, the recent development of nonthermal plasma techniques and nitrogen oxidation further provides abundant nitrate supply for the industrialized need.[9]

However, until now, large-scale eNO_3RR is limited by the low NH_3 selectivity and Faradaic efficiency (FE) due to the complex by-products in the eight-electron transfer process and the triggered competitive hydrogen evolution reaction (HER) when the applied bias reaches a specific size.[10–12] To this end, the binding strength of multi-absorbates on the active sites is decisive for the catalytic activity and selectivity. This strength determines the energy barriers during chemical reaction.[13–15] Due to the advent of nanotechnology, 2D materials have unveiled various excellent properties, including large specific areas; therefore, 2D materials are considered appropriate candidates for multiple catalytic reactions.[16–18] It is widely reported that the interlayer manipulation of 2D materials affects the chemical affinity of absorbates during electrocatalysis. For example, increasing the interlayer spacing of MoS_2 is beneficial for the HER activity because the enhanced spacing

D. Chen, S. Zhang, D. Yin, W. Li, X. Bu, Q. Quan, Z. Lai, W. Wang, Y. Meng, F. Chen, C. Zhi, J. C. Ho
Department of Materials Science and Engineering
City University of Hong Kong
Hong Kong SAR 999077, P. R. China
E-mail: johnnyho@cityu.edu.hk

W. Wang, Y. Meng, J. C. Ho
State Key Laboratory of Terahertz and Millimeter Waves
City University of Hong Kong
Hong Kong SAR 999077, P. R. China

C. Liu
Key Laboratory of Advanced Materials Processing & Mold
Zhengzhou University
Ministry of Education
Zhengzhou 450002, P. R. China

S. P. Yip, J. C. Ho
Institute for Materials Chemistry and Engineering
Kyushu University
Fukuoka 816-8580, Japan

The ORCID identification number(s) for the author(s) of this article can be found under https://doi.org/10.1002/aenm.202203201.

DOI: 10.1002/aenm.202203201

© 2022 Wiley-VCH GmbH

Check for updates
16146840, 2023, 6, Downloaded from https://onlinelibrary.wiley.com/doi/10.1002/aenm.202203201 by City University Of Hong Kong, Wiley Online Library on [14/03/2023]. See the Terms and Conditions (https://onlinelibrary.wiley.com/terms-and-conditions) on Wiley Online Library for rules of use; OA articles are governed by the applicable Creative Commons License

can weaken the van der Waals interaction and decouple the adjacent MoS_2 layers. This way, a lower Gibbs free energy of hydrogen adsorption (ΔG_{H^*}) would be resulted, facilitating the proton adsorption and desorption.[19] Moreover, the adjustment of interlayer spacing can not only tune the atomic distance and electron interaction but also manipulates the electronic structure of host materials, promising higher electrical conductivity.[20,21] Therefore, strategies for enlarging or shortening the interlayer spacing are very possible to modulate the binding strength of intermediates, such as NO_2^-, and the competitive HER process in eNO_3RR. Recently, active diatomic A-B pairs are a novel tool in structural regulation due to their strong interaction. Cerium (Ce), as a lanthanide series rare earth element, exhibits unique acid-base and redox properties, which can be a potential candidate to achieve support or promoter of noble metals (such as Pt, Rh, Pd).[22,23] For instance, many works apply Ce and their oxides as supporting materials for exceptionally stabilizing Pt single atoms.[24,25] Some works also facilitate the reaction process by means of the strong interaction of Pt-Ce pairs. Y. Shi et al. investigated the synergistic effect of Pt/Ce and USY zeolite in Pt-based catalysts with high activity for volatile organic compounds degradation. The strong interaction between Pt and Ce effectively inhibits the formation of by-products.[26] In this case, since Ce ions have already been used to increase the interlayer spacing of a graphene oxide membrane, harnessing the strong interaction of active diatomic Pt-Ce pairs to exert stain between the layers in 2D material is a feasible and promising technique to adjust the interlayer spacing.[27] Compared to the typical interlayer spacing engineering, such as chemical intercalation and physical compression, the conjunctive application of diatomic A-B pairs can achieve a bidirectional change in increasing and decreasing the interlayer spacing instead of a monodirectional change in the conventional scheme.

Inspired by the above works, we employ 2D SnS materials as an appealing candidate for eNO_3RR owing to the intrinsically poor surface electron accessibility inhibiting HER activity.[28] Through in-situ electrochemical reduction, the SnS nanosheets (NS) can be successfully converted from the SnS_2 NS. By introducing Ce and Pt into the lattices and spacings of the SnS NS successively, it achieves an expansion (from 5.672 ± 0.019 Å to 6.040 ± 0.034 Å) and shrinkage (from 5.898 ± 0.028 Å to 5.220 ± 0.031 Å) of the interlayer spacings. Taking together the DFT calculation and electrochemical in situ Raman spectroscopy, we found that the smaller spacings strengthen the p electron delocalization of Sn 5p orbitals. The delocalized electrons offer enhanced chemical affinity towards NO_3^- and NO_2^- but inhibit hydrogen generation simultaneously, promoting the rate-determining step (RDS) of $*NO_3 \rightarrow *NO_2$ in eNO_3RR and facilitating the conversion from NO_3^- to NH_3 for both activity and selectivity. The SnS NS with compressed interlayer spacing can achieve an NH_3 Faradaic efficiency of 94.12% and a high yield rate of 0.3026 mmol cm^{-2} h^{-1} at –0.5 V versus RHE. To the best of our knowledge, this interlayer spacing manipulation by using active diatomic pairs for eNO_3RR has never been reported; therefore, it opens a new pathway to design low-cost 2D catalysts with highly selective eNO_3RR activity.

2. Results and Discussion

2.1. Catalyst Design and Characterization

Since SnS is poor for HER process compared to SnS_2 owing to the puckered structure (**Figure 1**a), Gibbs free energy of hydrogen adsorption at all edges is disadvantageous for HER and thus becomes a promising candidate for eNO_3RR.[29] The SnS nanosheets (SS NS) synthesis is schematically illustrated in Figure 1a. SnS_2 nanosheets (SS_2 NS) were firstly grown on carbon cloth by facile hydrothermal method, and then electrochemically reduced into SS NS after cyclic voltammetry (CV) process in 1.0 M H_2SO_4 depicted as following Equation (1):

$$SnS_2 + H_2O + 2e^- \rightarrow SnS + HS^- + OH^- \quad (1)$$

Figure 1b shows the in situ Raman spectra during the conversion. Along with the increase of CV cycles, the Raman peaks associated with SnS_2 at around 313.4 cm^{-1} gradually become weak, replaced by the progressively reinforced A_g peaks located at 61.7, 95.8, 190.7 and 217.3 cm^{-1}, and B_g peak at 163.8 cm^{-1}, which all index to the SnS structure.[30] The morphology of SS maintains the typical nanosheet of SS_2, other than a little more deformation and a slightly increased thickness of the NS. (Figure 1c,d and Figure S1, Supporting Information). Through DFT calculation, the smaller bandgap of SS NS (0.958 eV) compared to SS_2 NS (1.404 eV) suggests a relatively high intrinsic conductivity.[31] Based on the X-ray diffraction (XRD) results in Figure S2 (Supporting Information), after CV cycles, the hexagonal SnS_2 phase with cell parameters of 3.6486 Å × 5.8992 Å (JCPDS card No.23-0677) converts into the orthorhombic SnS phase with cell parameters of 11.2 Å × 3.99 Å × 4.34 Å (JCPDS card No.65-3812). In the high-resolution transmission electron microscopy (HRTEM) images (Figure 1g,h), the characteristic lattice fringes of 1.748 Å corresponding to hexagonal SnS_2 (111) are observed, which is well differentiated from the typical lattice spacing of 2.936 Å assigned to orthorhombic SnS (011). These results prove the successful conversion from SnS_2 to SnS by in situ electrochemical reduction while keeping the flake structure and good crystallinity. Whereafter, active diatomic Pt-Ce pairs were used to regulate the interlayer spacing to study the influence on eNO_3RR. Ce atoms with different concentrations were first introduced into parallel SS_2 NS, which also offer the active sites for stabilizing monodispersed Pt atoms that profited from their strong interaction.[30] Pt atoms were then inserted by the CV process; in the meantime, SS_2 NS experience phase conversion and change into SS NS (See in Methods, Figures S3 and S4, Supporting Information). In **Figure 2**a–c, HRTEM images give the information on the interlayer spacing of the typical layer structure of SS, Ce doped SS (Ce_x-SS, x represents the atomic percent of Ce elements), and Pt-intercalated Ce doped SS (Pt_y/Ce_x-SS, y represents the atomic percent of Pt elements). The detailed ratios of Ce and Pt are summarized in Tables S1 and S2 (Supporting Information). It confirms that the fringes are about 5.672 Å by measuring the distance of adjacent SS NS. After Ce doping, the interlayer spacings expand from 5.858 Å of SS_2 NS to 6.030 Å of $Ce_{0.5}$-SS_2 due to the electron

© 2022 Wiley-VCH GmbH

16146840, 2023, 6, Downloaded from https://onlinelibrary.wiley.com/doi/10.1002/aenm.202203201 by City University Of Hong Kong, Wiley Online Library on [14/03/2023]. See the Terms and Conditions (https://onlinelibrary.wiley.com/terms-and-conditions) on Wiley Online Library for rules of use; OA articles are governed by the applicable Creative Commons License

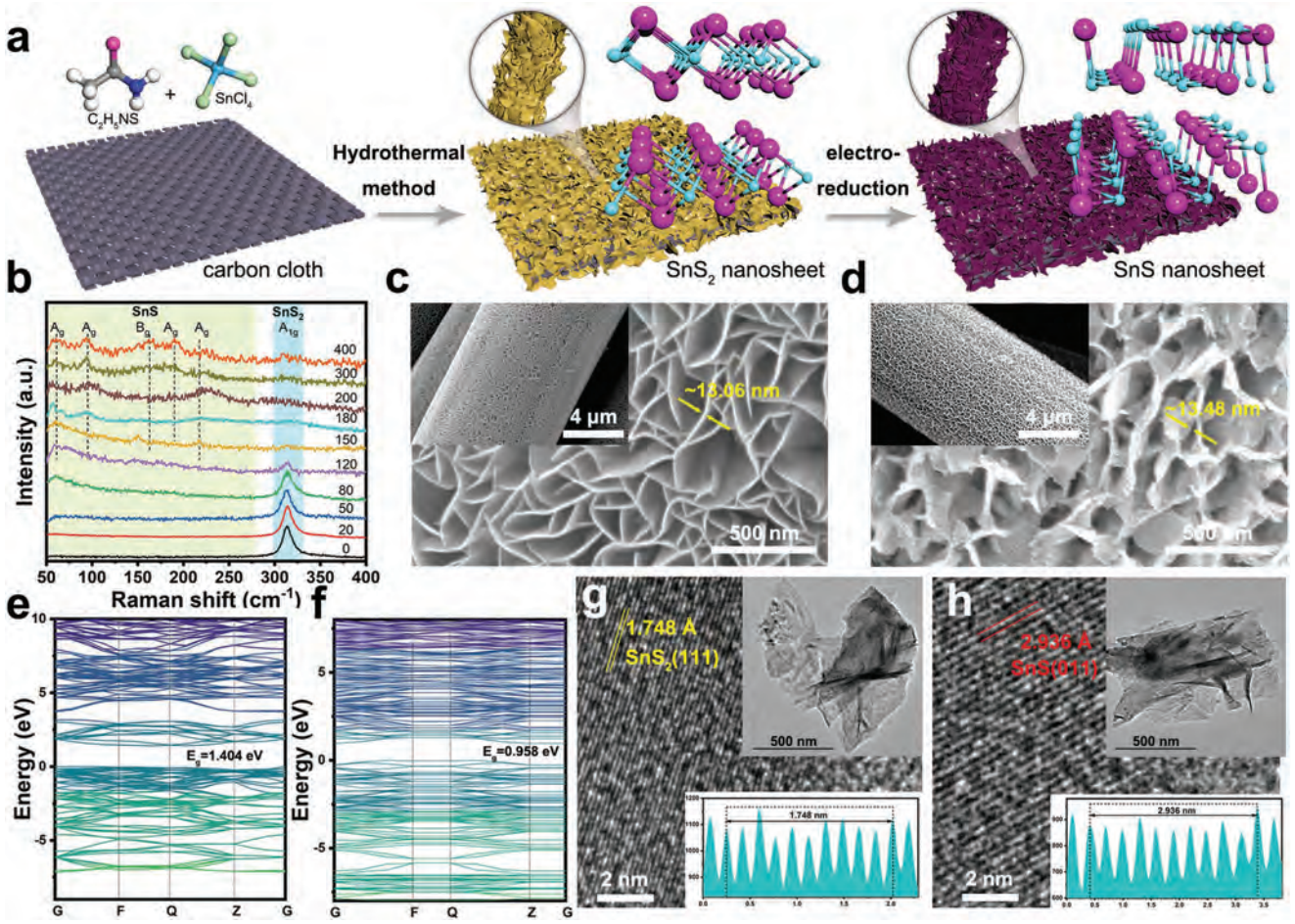

Figure 1. In situ electrochemical conversion of SnS_2 NS into SnS NS. a) Schematic illustration of the fabrication procedure for SnS NS. b) In situ Raman spectra during the electrochemical conversion process from SnS_2 to SnS. SEM images of c) SnS_2 and d) SnS. The inset figures are the SEM images at lower magnification. Calculated band structures of e) SnS_2 and f) SnS. E_g represents the bandgap. HRTEM images of g) SnS_2 and h) SnS. The upper insets are the TEM images, and the bottom ones are the intensity profile that shows the corresponding lattice fringes.

transfer from Ce to the antibonding of SnS_2 that increases the repulsive force between adjacent layers (Figures S5 and S6, Supporting Information), which will be further proved in following experiments. Such expansive behavior decreases slightly after the phase conversion from SS_2 NS to SS NS but remains larger than un-doped SS NS (Figure 2b). The single Pt atoms were then intercalated into the interlayer of $Ce_{0.5}$-SS_2 by the CV process. Unlike conventional chemical insertion in previous works, such as inserting graphene between SnS_2 nanosheets and intercalating tetrabutylammonium into the interlayer of 2H-MoS_2 nanosheets, which both enlarge the interlayer spacing, the embeddedness of metal atoms in our work leads to the compression of interlayer spacing rather than the expansion.[32,33] This is attributed to the strong interaction of active diatomic Pt-Ce pairs, which could enhance the forces of adjacent layers, thus closing the distance between SS layers.[34] The compressed interlayer spacing of $Pt_{0.9}/Ce_{0.5}$-SS is determined as ≈5.434 Å in Figure 2c. Figure S7 and Table S3 (Supporting Information) present the average interlayer spacing values collected from over ten different locations in each sample. The detailed statistical process of SS, $Ce_{0.5}$-SS and $Pt_{0.9}/Ce_{0.5}$-SS, the main discussion objects, are shown in Figures S8–S10 (Supporting Information). Along with the increased concentration of Ce and Pt elements, it exhibits an excellent linear relationship. When the Ce concentration elevates from 0% to 1.0%, the interlayer spacing in SS NS achieves an increase from 5.672 ± 0.019 Å to 6.040 ± 0.034 Å. As for Pt intercalation, the interlayer spacing could be gradually reduced to 5.220 ± 0.031 Å with the increasing CV cycles, even below the value of intrinsic SS NS. Therefore, upon the regulation of active diatomic Pt-Ce pairs, we successfully tune the interlayer coupling of 2D SS NS and realize the interlayer spacing changes from 5.220 ± 0.031 to 6.040 ± 0.034 Å, which indicates a variation range from 6.49% to 7.97% compared to the intrinsic value of SS NS.

In Figure 2d and Figure S11 (Supporting Information), the typical TEM image of $Pt_{0.9}/Ce_{0.5}$-SS and SEM images of the catalysts with different Pt concentrations illustrate the flake structure similar to the initial SS NS. This observation suggests that Ce doping and Pt insertion process have no significant effect on the NS morphology. The corresponding STEM, EDX mapping and EDX spectra reveal strong Sn and S signals well-distributed in the entire nanosheet and a weak signal of Pt and Ce, which indicates the successful introduction of Pt-Ce atoms (Figure 2e and Figure S12, Supporting Information). Similar to the phase

© 2022 Wiley-VCH GmbH

16146840, 2023, 6, Downloaded from https://onlinelibrary.wiley.com/doi/10.1002/aenm.202203201 by City University Of Hong Kong, Wiley Online Library on [14/03/2023]. See the Terms and Conditions (https://onlinelibrary.wiley.com/terms-and-conditions) on Wiley Online Library for rules of use; OA articles are governed by the applicable Creative Commons License

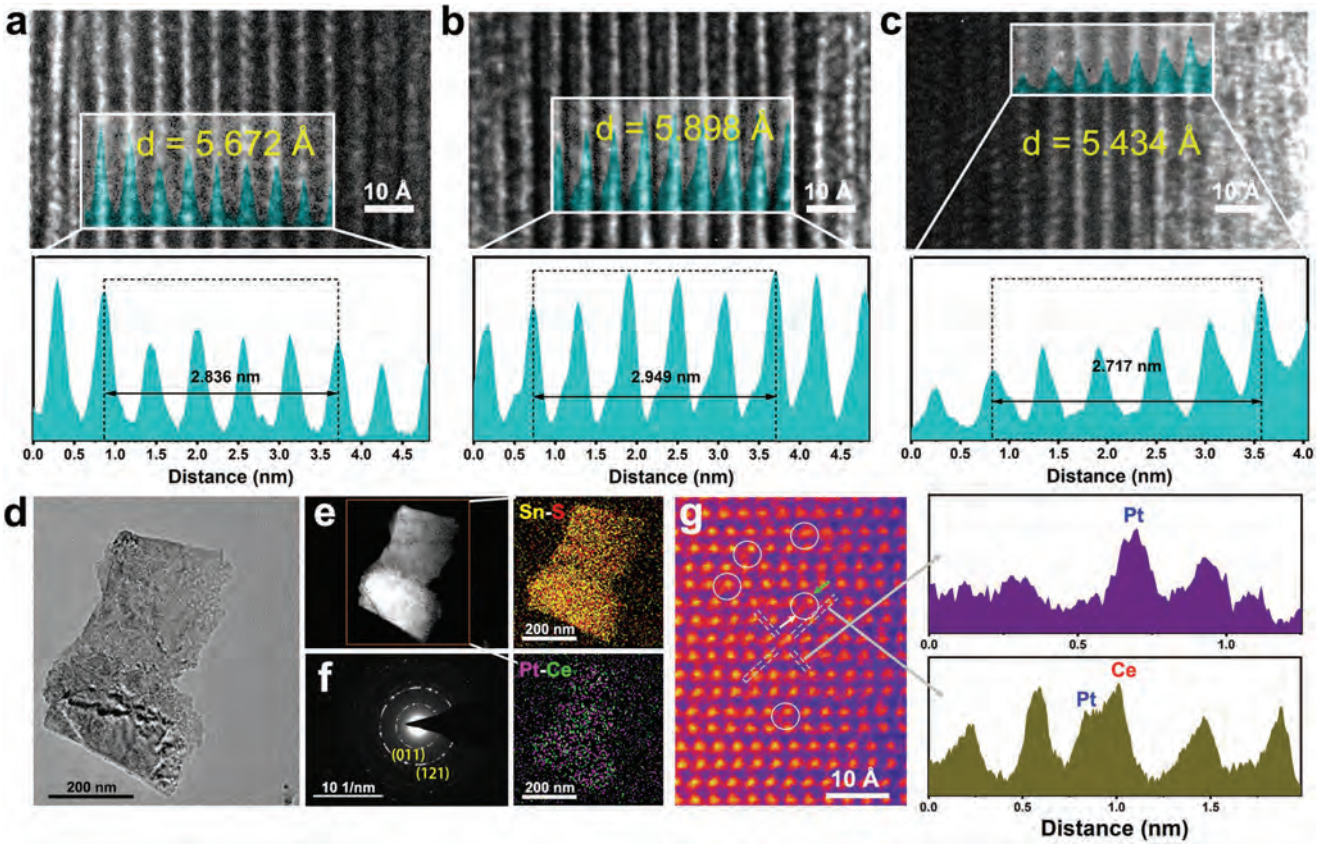

Figure 2. Interlayer modulation of SnS NS by adopting active diatomic Pt-Ce pairs. HRTEM images of the layered edges of a) SS, b) $Ce_{0.5}$-SS, and c) $Pt_{0.9}/Ce_{0.5}$-SS and the intensity profiles in the bottom panels corresponding to the areas marked by white rectangles in the upper panels. Typical d) TEM image, e) STEM image, d) EDX mappings, and f) SAED pattern of $Pt_{0.9}/Ce_{0.5}$-SS. g) Atomic-resolution HAADF-STEM image of $Pt_{0.9}/Ce_{0.5}$-SS and the corresponding line intensity profiles in the selected regions marked by the gray dashed line. The green and white arrows point to the Ce and Pt atom, respectively.

transition from pure SnS_2 to SnS, for $Ce_{0.5}$-SS_2, the hexagonal SnS_2 phase also gradually converts into the orthorhombic SnS phase, but no signal peaks of Pt- or Ce-based compounds are observed in the XRD patterns (Figure S13, Supporting Information). Moreover, the selected area electron diffraction (SAED) of $Pt_{0.9}/Ce_{0.5}$-SS in Figure 2f also has only the typical annulus pattern indexed to polycrystalline SnS with (011) and (121) diffraction planes. Then, atomic-resolution HAADF-STEM images illuminate the effect of active diatomic Pt-Ce pairs exerted on SnS NS. It is noteworthy that in the HAADF-STEM image of $Pt_{0.9}/Ce_{0.5}$-SS (Figure 2g), some interstitial atoms appear in pair with the atoms in the lattice, which are thought to be Pt and Ce.[34] Since no extra atoms exist in the interplanar in $Ce_{0.5}$-SS (Figure S14, Supporting Information) and only atoms with a relatively higher intensity profile occur in the lattice, the green circled atoms occupied the Sn site in SnS could be assigned to Ce. Therefore, regarding $Pt_{0.9}/Ce_{0.5}$-SS, the interstitial atoms pointed by white arrow could be Pt atoms. The different brightness of these interstitial atoms may be ascribed to various heights compared to the measured surface. As a result, in diatomic Pt-Ce affected SS NS, Ce atoms are doped by substituting Sn on Sn sites, while Pt single atoms are intercalated into SS NS and stabilized by Ce, which will be further proved by the following measurements. Considering that the intercalated Pt atoms can probably lie on both surface or interplanar of the Ce_x-SS, we calculate the adsorption energy of Pt single atom on Ce_x-SS at different positions (Figure S15 and Table S4, Supporting Information). Among the four situations, position "a" has the smallest adsorption energy, which is selected as the model for following DFT calculations. Furthermore, in order to evaluate the role of Ce toward Pt, we synthesize $Pt_{1.2}$-SS without Ce doping. It is evident that Pt atoms tend to aggregate to form nanoparticles without stabilizing with Ce atoms (Figure S16, Supporting Information). The lattice fringes of 0.23 nm correspond to the (111) plane of Pt nanoparticles. More importantly, the aggregated Pt nanoparticles lead to the expansion of interlayer spacing unavoidably due to the swell effect (Figure S16d,e, Supporting Information), which is coincident with previous reports that the introduction of metal ions in 2D materials would cause the expansion of interlayer spacing and increase of Fermi energy levels and band gaps owing to the extra free electrons.[35] As such, Ce atoms play an essential role in stabilizing the Pt single atoms in this system. Only through the coexistence of Pt-Ce pairs can the compression of the interlayer spacing be realized.

2.2. Chemical Environment Variation in the Interlayer Spacing Modulation

Since catalytic behaviors of materials, to a great extent, are determined by the local electronic structure and chemical

© 2022 Wiley-VCH GmbH

16146840, 2023, 6, Downloaded from https://onlinelibrary.wiley.com/doi/10.1002/aenm.202203201 by City University Of Hong Kong, Wiley Online Library on [14/03/2023]. See the Terms and Conditions (https://onlinelibrary.wiley.com/terms-and-conditions) on Wiley Online Library for rules of use; OA articles are governed by the applicable Creative Commons License

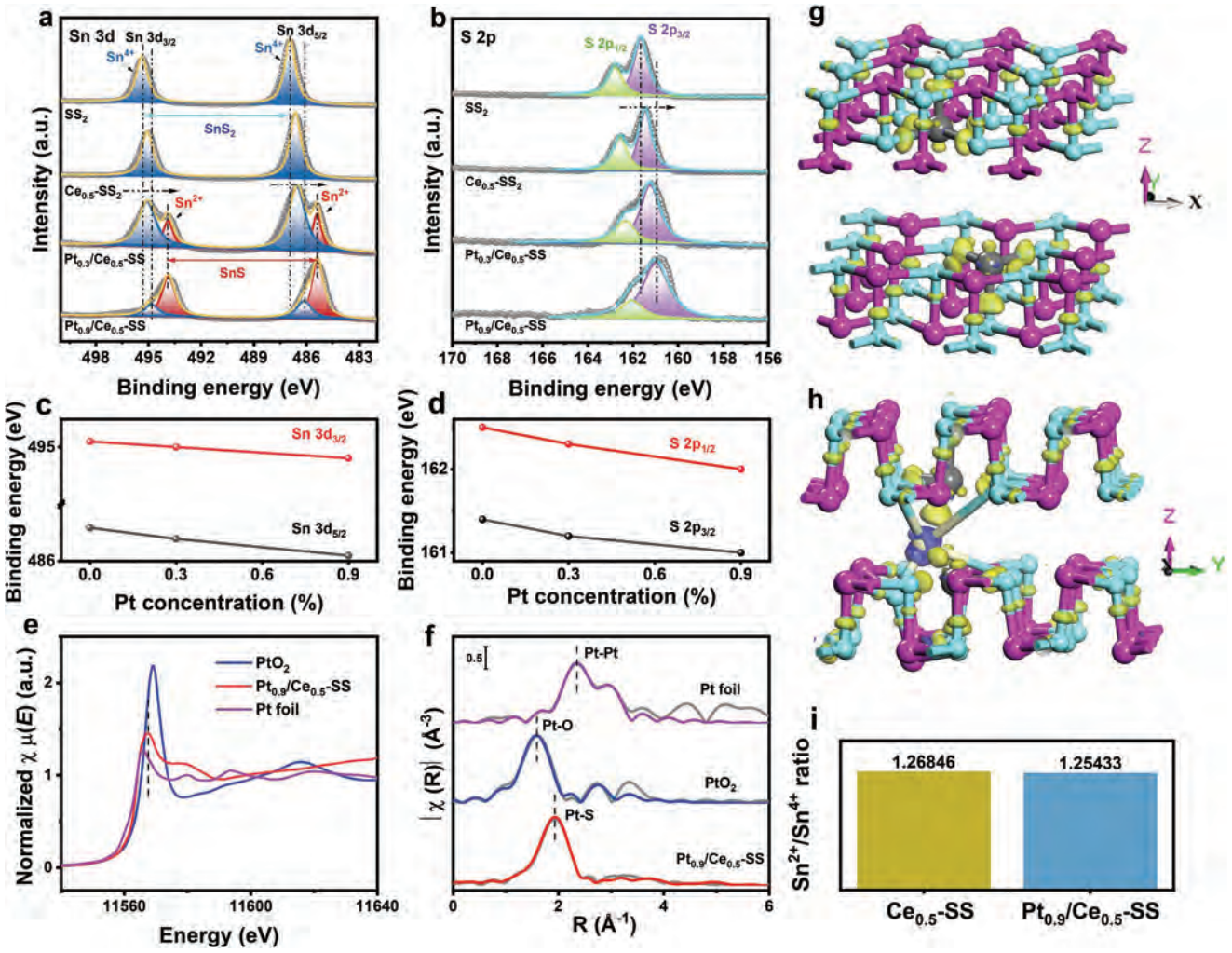

Figure 3. The local chemical environment of the interlayer-spacing-regulated samples. XPS survey spectra of a) Sn 3d and b) S 2p. The binding energy variation of c) Sn 3d and d) S 2p with the increasing Pt concentration. Pt L_{III}-edge of e) the normalized XANES spectra and f) Fourier transform of k^2-weighted EXAFS spectra of $Pt_{0.9}/Ce_{0.5}$-SS and reference Pt foil and PtO_2. Charge density difference of g) Ce_x-SS and h) Pt_y/Ce_x-SS. The azure, mauve, gray and white balls refer to S, Sn, Ce, and Pt atoms. Yellow and blue isosurfaces represent charge accumulation and depletion around Ce and Pt atoms, respectively. i) The ratio of Sn^{2+}/Sn^{4+} obtained from XPS results of $Ce_{0.5}$-SS and $Pt_{0.9}/Ce_{0.5}$-SS.

environment, X-ray photoelectron spectroscopy (XPS) was used to analyze the change of chemical states and local structures caused by Pt-Ce diatoms in adjusting the interlayer spacing.[36] Table S5 (Supporting Information) summarizes the detailed values of binding energies of the catalysts. As depicted in **Figure 3**a, the binding energies of the characteristic peaks of Sn^{4+} are downshifted after introducing Ce atoms, indicating that the in-plane doping of Ce does not change the chemical state of Sn but can cause the electron transfer to the host materials of SnS_2.[37] Basically, such doping-induced electrons would make a repulsive force between adjacent anti-orbitals of Sn-S, resulting in a large distance between planes, as we discovered in the HRTEM results.[38] The similar binding energy in $Ce_{0.5}$-SS with $Ce_{0.5}$-SS_2 illustrates that Ce doping has no significant role during the phase change (Figure S17, Supporting Information). With the intercalation of Pt single atoms, for one thing, Sn^{2+} begins to appear and gradually increases as the Pt concentration goes up, proving the phase transformation from SnS_2 to SnS. For another thing, because Pt has a lower electronegativity than SnS owing to the large electronegativity of nonmetallic element S, the binding energies of Sn 3d further shift to lower values after Pt intercalation. In Figure 3b, XPS spectra of S 2p can be deconvoluted into peaks of S $2p_{1/2}$ and $2p_{3/2}$, corresponding to S^{2-}.[39] For a clear comparison, the line graph in Figure 3c,d show the binding energy variation of Sn 3d and S 2p. Both binding energies have a downward tendency with the increasing Pt concentration, confirming the electrons transfer from Pt to the host materials of SnS. X-ray absorption near-edge structures (XANES) of the Pt L_{III}-edge for $Pt_{0.9}/Ce_{0.5}$-SS and the reference sample Pt foil and PtO_2 are shown in Figure 3e. The energy of absorption edge and the height of white-line are higher than those of Pt foil but lower than PtO_2, which demonstrates the electrons flow from Pt atoms to SnS. Additionally, the electrons transfer also affects the valence states of Ce, as evidenced by the larger portion of v' + u' (≈19.31%) that index to III valence to the area of all the peaks in $Pt_{0.9}/Ce_{0.5}$-SS

© 2022 Wiley-VCH GmbH

16146840, 2023, 6, Downloaded from https://onlinelibrary.wiley.com/doi/10.1002/aenm.202203201 by City University Of Hong Kong, Wiley Online Library on [14/03/2023]. See the Terms and Conditions (https://onlinelibrary.wiley.com/terms-and-conditions) on Wiley Online Library for rules of use; OA articles are governed by the applicable Creative Commons License

than that for $Ce_{0.5}$-SS (≈8.00%), while others index to IV valence (Figure S18, Supporting Information).[40] These phenomena suggest that the incoming Ce and Pt in 2D SnS lead to the local chemical environment variation, more than adjusting the interlayer spacing, which probably influences the catalytic property in eNO_3RR. Furthermore, extended X-ray absorption fine structure (EXAFS) at Pt L_{III}-edge and the fitting results (Figure 3f, Figure S19 and Table S6, Supporting Information) indicate the atomically dispersed Pt, with only Pt-S coordination structure in the first coordination shell and no evidence of a Pt-Pt scattering path in the spectra, which clearly prove that Pt is intercalated as a single atom into the SS. This result is consistent with the XPS spectra of Pt 4f, where the main peaks in $Pt_{0.9}/Ce_{0.5}$-SS at ≈72.8 and 76.1 eV are assigned to Pt^{2+}, corresponding to the characteristic peak positions of Pt-S bonds (Figure S20, Supporting Information). This way, $Pt_{1.2}$-SS have a large percentage of Pt^0, emphasizing that Ce stabilizes Pt single atom to prevent Pt nanoparticles from evolving (Figures S20 and S21, Supporting Information). The very close ratio of Sn^{2+}/Sn^{4+} in Figure 3i means that Pt only exerts influence on electron transfer but not on the valence state components of Sn, further confirming that Pt single atoms are intercalated into 2D SS NS rather than doping. Therefore, although the intercalation of Pt also brings extra negative electrons, the strong diatomic Pt-Ce interaction promotes the formation of Pt-S bonds, enhancing the interlayer force and shortening the interlayer spacing. At the same time, DFT calculation was applied to study the interlayer spacing variation and electronic structure to gain further insights. To simulate the actual situation of the catalysts, we set the initial interlayer spacing of SS NS as 5.67 Å. The calculated models after geometrical optimization show the interlayer spacing of 5.67, 5.89, and 3.68 Å for SS, Ce_x-SS, and Pt_y/Ce_x-SS, respectively (Figure S4, Supporting Information), in accidence with the interlayer spacing variation in experimental results. Also, the charge density difference images (Figure 3g, h) further reveal a more robust charge redistribution around the Ce and Pt locations, which proves the electron transfer and the increase of internal electron concentration, thus enhancing the catalytic activity.[41] The electrochemical impedance spectroscopy (EIS) result shows that $Pt_{0.9}/Ce_{0.5}$-SS exhibit a considerably smaller charge transfer resistance of 119.6 Ω as compared to SS (253.1 Ω) and $Ce_{0.5}$-SS (293.5 Ω), indicating the obviously improved reaction kinetics of the electrodes with smaller interlayer spacing (Figure S22, Supporting Information).[42]

2.3. Electrocatalytic eNO3RR Performance

Upon possessing the 2D SS NS materials with adjustable interlayer spacings, we then evaluate their electrocatalytic performance for NO_3^--to-NH_3 conversion. The eNO_3RR performance was performed in an H-type cell under ambient conditions in 0.5 M Na_2SO_4 (pH adjusted to 11.5) with 0.1 M KNO_3 as a nitrate source. There are two reasons for adjusting the pH of the Na_2SO_4 solution. One reason is that the pH of the initial unbuffered electrolyte would change from neutral to ≈11 owing to the gradually consumed H^+ along with eNO_3RR and competitive HER. The other reason is that the alkaline media prevents the further reduction of SnS under negative potential according to Equation (1), inhibiting the component variation.[9,43] Therefore, adjusting the pH of the Na_2SO_4 solution can keep the stability of both pH and catalyst composition. Linear sweep voltammetry (LSV) curves exhibit the current density of SS, $Ce_{0.5}$-SS, and $Pt_{0.9}/Ce_{0.5}$-SS with and without NO_3^- (**Figure 4**a), in which the low current response of catalysts without the existence of NO_3^- indicates the intrinsic poor hydrogen evolution, resulting from the limited surface electron accessibility of Sn.[44,45] As anticipated, the current density of catalysts shows a negative correlation with the gap of interlayer spacings. $Pt_{0.9}/Ce_{0.5}$-SS with the smaller interlayer spacing have a higher current density over a wide range of negative potentials and more positive onset potential, indicating more readily the reduction of NO_3^-. Furthermore, there are apparent reduction peaks within the presence of NO_3^-. The drastic increase in the current density indicates the fast nitrate reduction rate. With the potential becoming more negative, competitive hydrogen evolution gradually occurs but is still weaker than eNO_3RR, which leads to a gentler increase rate and forms the plateaus and inflection points. Until HER dominates, the current densities rapidly rise again, especially when the potential is more than –0.7 V versus RHE. Then, possible products, including NH_3, NO_2^-, and N_2H_4, are detected using the colorimetric method (Figures S23–S25, Supporting Information), which illustrates that NH_3 and NO_2^- are the main products during eNO_3RR in this system, and the yield of N_2H_4 is negligible. As depicted in Figure 4b, the steady increase of Faradaic efficiency (FE) of ammonia up to –0.5 V versus RHE, and the deterioration at more negative potential could result from the enhanced competing HER.[46] It can be seen that $Pt_{0.9}/Ce_{0.5}$-SS offer a FE of NH_3 of 94.12%, with a yield rate for NH_3 (Y_{NH3}) of 0.3056 mmol cm^{-2} h^{-1} at –0.5 V versus RHE (Figure 4b,c), 1.89 and 1.58-fold of $Ce_{0.5}$-SS (49.67%) and SS (59.35%), respectively. In particular, such multiple of FE increment is more evident in the potential range in –0.2 to –0.5 V, indicating the more easily motivation for NO_3^--to-NH_3 conversion of $Pt_{0.9}/Ce_{0.5}$-SS in smaller energy consumption, which is promising for industrial-scale applications. Furthermore, benefiting from the great FE of NH_3 of $Pt_{0.9}/Ce_{0.5}$-SS, it could reach a partial current density of NH_3 of 109 mA cm^{-2} at –0.8 V versus RHE much higher than that of $Ce_{0.5}$-SS and SS NS (Figure 4d). The above results suggest the critical role of interlayer spacing regulation in modulating the eNO_3RR performance, of which the compression of interlayer spacing under the assistance of active diatomic Pt-Ce pairs drastically promotes the FE and generation rate of NH_3. Specifically, the improvement of eNO_3RR performance is derived from the chemical reaction kinetic equilibrium rather than mass transfer, as evidenced by the substantially unchanged LSV curves and FE of NH_3 and NO_2^- products under different stir rates (Figure S26, Supporting Information).[46] To derive the intrinsic activities of the catalysts, we normalize the performance by the electrochemical active surface area (ECSA) (correlated with the double-layer capacity (C_{dl}), assuming 40 μF cm^{-2} as a moderate value for specific capacitance of a flat surface) in Figure S27 (Supporting Information).[47] The normalized partial current density of NH_3 suggest the high intrinsic eNO_3RR performance of $Pt_{0.9}/Ce_{0.5}$-SS. Furthermore, we measured the Zeta potential of SS, $Ce_{0.5}$-SS, and $Pt_{0.9}/Ce_{0.5}$-SS at pH = 10 to detect the surface electronic state. It exhibits an average Zeta potential

© 2022 Wiley-VCH GmbH

16146840, 2023, 6, Downloaded from https://onlinelibrary.wiley.com/doi/10.1002/aenm.202203201 by City University Of Hong Kong, Wiley Online Library on [14/03/2023]. See the Terms and Conditions (https://onlinelibrary.wiley.com/terms-and-conditions) on Wiley Online Library for rules of use; OA articles are governed by the applicable Creative Commons License

16146840, 2023, 6, Downloaded from https://onlinelibrary.wiley.com/doi/10.1002/aenm.202203201 by City University Of Hong Kong, Wiley Online Library on [14/03/2023]. See the Terms and Conditions (https://onlinelibrary.wiley.com/terms-and-conditions) on Wiley Online Library for rules of use; OA articles are governed by the applicable Creative Commons License

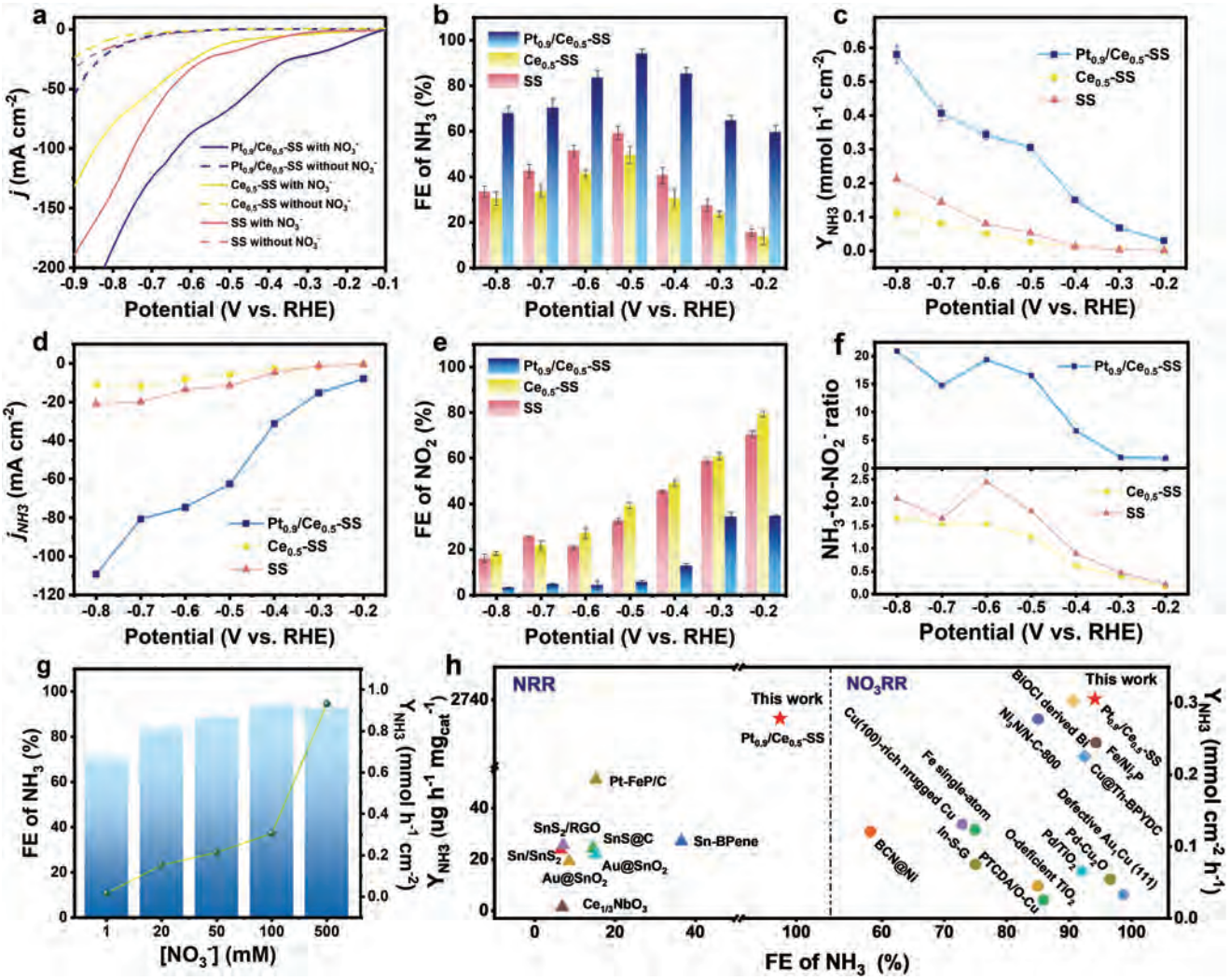

Figure 4. Electrocatalytic NO_3^--to-NH_3 conversion. a) LSV curves at a scan rate of 5 mV s^{-1} with and without NO_3^-. b) Faradaic efficiencies (FE) for NH_3. c) Yield rate for NH_3 (Y_{NH3}). d) Partial current densities of NH_3 (j_{NH3}). e) FE for NO_2^-. f) The NH_3-to-NO_2^- product ratios variation of SS, $Ce_{0.5}$-SS, and $Pt_{0.9}/Ce_{0.5}$-SS. g) FE and yield rate of NH_3 for $Pt_{0.9}/Ce_{0.5}$-SS in the electrolyte with different concentrations of NO_3^- ($[NO_3^-]$) at 0.5 V versus RHE. h) Comparison of Y_{NH3} and FE of $Pt_{0.9}/Ce_{0.5}$-SS with the recently reported representatives eNO_3RR and eNRR electrocatalysts (see the Supporting Information for detailed references).

of −45.78 mV of $Pt_{0.9}/Ce_{0.5}$-SS, −55.26 mV of SS and −60.60 mV of $Ce_{0.5}$-SS. Although the samples all show the negative surface charge in an aqueous KCl solution (pH = 10), the $Pt_{0.9}/Ce_{0.5}$-SS provides a much more favorable surface environment for nitrate adsorption.

Electrocatalytic NO_3RR follows a consecutive eight-electron pathway, where NO_2^- is an important by-product after a two-electron transfer process ($NO_3^- + 2e^- + H_2O \rightarrow NO_2^- + 2OH^-$).[48,49] This way, the rapid successive conversion rates for NO_3^--to-NO_2^- and NO_2^--to-NH_3 are critical for the efficiency of eNO_3RR. Consequently, we evaluate the production rate of NO_2^- during eNO_3RR, of which the FE of NO_2^- displays the opposite situation as NH_3 (Figure 4b,e and Figure S28, Supporting Information). $Ce_{0.5}$-SS with a bigger interlayer spacing show a higher FE of NO_2^-, while $Pt_{0.9}/Ce_{0.5}$-SS with compressed interlayer spacing exhibit unfavorable NO_2^- generation. Also, the further increase of cathodic potential leads to a generally continuous decline of the nitrite FE but the increase of ammonia FE of $Pt_{0.9}/Ce_{0.5}$-SS especially when the potential is smaller than −0.5 V versus RHE, indicating the possible fast reaction of NO_2^--to-NH_3 conversion. To validate it, we performed the LSV of $Ce_{0.5}$-SS and $Pt_{0.9}/Ce_{0.5}$-SS in the electrolyte with 0.1 M NO_2^- and with 0.1 M NO_3^-, respectively, and compared the FE of NH_3 during NO_2^- reduction reaction (NO_2RR) and NO_3^- reduction reaction (NO_3RR) (Figure S29, Supporting Information). The rapid increase of current density in NO_2RR of both $Ce_{0.5}$-SS and $Pt_{0.9}/Ce_{0.5}$-SS indicates the fast electrocatalytic reduction of NO_2^-. The Y_{NH3} value can reach 1.37 mmol cm^{-2} h^{-1} for $Pt_{0.9}/Ce_{0.5}$-SS and 0.57 mmol cm^{-2} h^{-1} for $Ce_{0.5}$-SS at −0.8 V versus RHE. However, the difference between FE NO_3RR and NO_2RR in $Ce_{0.5}$-SS is huge, especially at the smaller potential. For $Pt_{0.9}/Ce_{0.5}$-SS, the FEs keep a much smaller difference (Figure S29c,d,

© 2022 Wiley-VCH GmbH

16146840, 2023, 6, Downloaded from https://onlinelibrary.wiley.com/doi/10.1002/aenm.202203201 by City University Of Hong Kong, Wiley Online Library on [14/03/2023]. See the Terms and Conditions (https://onlinelibrary.wiley.com/terms-and-conditions) on Wiley Online Library for rules of use; OA articles are governed by the applicable Creative Commons License

Supporting Information), which confirms the fast NO_3^--to-NO_2^- reduction but subsequent desorption of NO_2^- to the electrolyte for $Ce_{0.5}$-SS, leading to the observed higher generation of NO_2^- in Figure 4e. Furthermore, the high NH_3-to-NO_2^- product ratio variation in Figure 4f verifies the stronger desorption of NO_2^- intermediates in $Ce_{0.5}$-SS and SS NS compared to $Pt_{0.9}/Ce_{0.5}$-SS. This finding reveals that the interlayer spacing regulation plays a vital role in chemical affinity towards NO_2^- that affects the reduction from NO_2^- to NH_3 and the entire activity and selectivity of eNO_3RR.

To further evaluate the eNO_3RR performance of the catalysts, we study the influence of nitrate concentration ($[NO_3^-]$) on $Pt_{0.9}/Ce_{0.5}$-SS, in which the ammonia FE maintains a high value of more than 70% from 0.001 to 0.5 M and reaches to the peak at 0.1 M. As reported, the competing HER could be suppressed by increasing $[NO_3^-]$ and/or the pH value of electrolytes.[50] Notably, the $Pt_{0.9}/Ce_{0.5}$-SS show a decreased ammonia FE along with a reduced $[NO_3^-]$, indicating that the eNO_3RR on $Pt_{0.9}/Ce_{0.5}$-SS is challenged by the enhanced hydrogen evolution. However, there are two possible explanations for the minor decline in ammonia FE when $[NO_3^-] > 0.1$ M. One explanation is that too high $[NO_3^-]$ is favorable for the desorption of NO_2^- from active sites, resulting in the increased generation of NO_2^-. The other reason is the deactivation of active sites due to the slow mass transfer of a large amount of produced ammonia.[9,21] Besides, to confirm the origin of the detected NH_3, isotope labeling experiments were conducted in the presence of $^{14}NO_3^-$ or $^{15}NO_3^-$ followed by product identification and quantification via ^1H NMR (Figures S30 and S31, Supporting Information). The standard $^{14}NH_4^+$ solution is split into three characteristic peaks, while that for $^{15}NH_4^+$ shows two peaks. As a result, there is no signal of the original $^{14}NO_3^-$ or $^{15}NO_3^-$ electrolyte until they experience electrocatalytic nitrate reduction, and the signal peaks are basically the same as the standard $^{14}NH_4^+$ and $^{15}NH_4^+$. In addition, the FE of ammonia and Y_{NH3} are quantitated by NMR using ^{15}N isotope labeled nitrate as the reactant. By comparing with the calibration curve, the results are very close to those determined by the UV–vis method, as shown in Figure S31b (Supporting Information), thus excluding the possibility of environmental contaminants influencing the detection results. Finally, the gradually enhanced eNO_3RR performance and the compressed interlayer spacing from $Ce_{0.5}$-SS to $Pt_{0.3}/Ce_{0.5}$-SS, and to $Pt_{0.9}/Ce_{0.5}$-SS directly suggest the catalytic role of interlayer spacing regulation toward nitrate reduction (Figure S32, Supporting Information). However, the higher concentration of Pt may promote the competing HER activity that inhibits the ammonia selectivity, considering that Pt is an excellent active site for HER.[51] Thereby, $Pt_{1.2}/Ce_{0.5}$-SS and $Pt_{1.2}$-SS exbibit decreased performance in eNO_3RR, even if the interlayer spacing of $Pt_{1.2}/Ce_{0.5}$-SS is very small. These results endow the proposed interlayer spacing engineering on 2D SnS nanosheets through adopting active diatomic Pt-Ce pairs, showing superior FE and yield rate of NH_3, and ranking among the most NH_3 synthesizing electrocatalysts (Figure 4h and Table S7, Supporting Information). The several orders of magnitude higher in NH_3 production also confirm the practical potential of NO_3^- reduction compared to N_2 reduction.

2.4. Understanding the Enhanced eNO3RR Performance on Pty/Cex-SS NS

Then, we sought to understand the origin of the remarkable performance of $Pt_{0.9}/Ce_{0.5}$-SS for eNO_3RR. Firstly, in-situ Raman spectroscopy was applied to monitor the possible reaction intermediates or products under potentiostatic operation for 1 h at –0.5 V versus RHE (**Figure 5**a). Except for the two peaks at about 1352.0 and 1590.5 cm^{-1} assigned to the D-peak and G-peak of carbon cloth, the peaks at 1152.5 and 1521.4 cm^{-1} gradually appeared on $Pt_{0.9}/Ce_{0.5}$-SS as the reaction progressed, which could be attributed to the stretching of H-N-H and N-H bond, respectively.[52,53] This indicates the efficient nitrate reduction to ammonia on the $Pt_{0.9}/Ce_{0.5}$-SS electrode. More directly, the gradually enhanced peak intensity of H-N-H and N-H peaks in contour plots in Figure 5b,c provides strong evidence of increased intermediates. It is well known that transition metals' versatile d-orbital electron states regulate the ability to adsorb intermediates as described in d-band theory.[54] Many works prove that the enhanced catalytic activity of transition metals results from the delocalized d electrons.[55,56] Consequently, for main-group metals, such as Sn and Bi, even though they do not show diversity in d-orbital, they have various localized p-orbital electron states, making it reasonable to hypothesize that the p-orbital electron states would also affect their catalytic performance. Therefore, we compute the electronic structures of SS, Ce_x-SS, and Pt_y/Ce_x-SS models by DFT calculation. As depicted in Figure 5d, the computed PDOS diagrams of Sn 5p orbitals show an evident delocalization effect, especially for Pt_y/Ce_x-SS. As we know that Ce_x-SS, SS, and Pt_y/Ce_x-SS have an ordinal decreasing interlayer spacing after geometric optimization (Figure S4, Supporting Information), we found the degree of p-orbital electron delocalization is negatively correlated with the value of interlayer spacing. Specifically, Pt_y/Ce_x-SS with compressed interlayer spacing may lead to an enhanced coupling of electrons in real space, which is responsible for delocalizing electrons across Sn-p orbitals.[57] As a result, such electron delocalization may play a significant role in altering the electronic interaction of absorbates.[58] To shed more light on this, we built the model of NO_3^- that adsorbed on previous SS, Ce_x-SS, and Pt_y/Ce_x-SS models and computed the PDOS of Sn-5p and O-2p orbitals (Figure 5e). Evidently, a greater orbital hybridization around the Fermi level (E_F) is recognizable between the Sn atom and adsorbed NO_3^-, indicating enhanced chemical interaction. Subsequently, the difference between the band center (ε) of Sn-5p and O-2p orbitals exhibits a linear relationship with the interlayer spacing, of which Pt_y/Ce_x-SS have the smallest value of 3.2650 eV, lower than those of SS (3.3074 eV), and Ce_x-SS (3.3663 eV). Hence, the narrower band center difference demonstrates the crucial function of interlayer spacing regulation in weakening and activating the N=O bonds of NO_3^-. Furthermore, in Figure 5f, Ce_x-SS, SS, and Pt_y/Ce_x-SS with gradually compressed interlayer spacing reveal promoted adsorption energy (ΔE) of NO_3^- and NO_2^-, suggesting the enhanced chemical affinity towards NO_3^- and NO_2^- and further prove the reliable effect of interlayer spacing regulation. It is also noted that the $\Delta E_{NO_2^-}$ of Pt_y/Ce_x-SS reaches –1.58 eV, while that for Ce_x-SS only has a value of –1.18 eV. The stronger adsorption of NO_2^- inhibits the generation of HNO_2 by-product

© 2022 Wiley-VCH GmbH

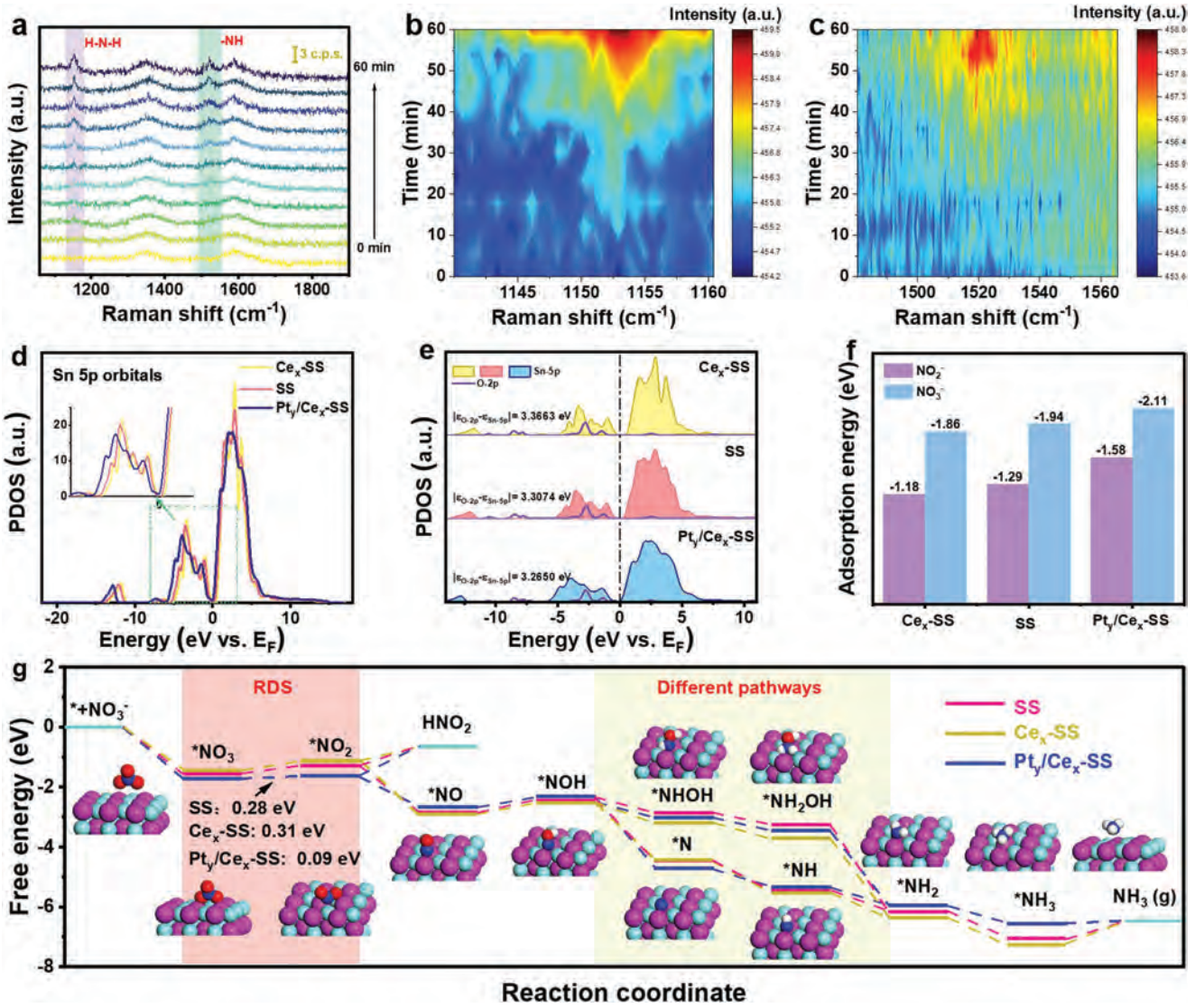

Figure 5. Mechanism of performance improvement of $Pt_{0.9}/Ce_{0.5}$-SS. a) In situ Raman spectra of $Pt_{0.9}/Ce_{0.5}$-SS collected at −0.5 V versus RHE in NO_3^--contained solution. b, c) Corresponding contour plots of the color background area in a). d) The computed PDOS diagrams of Sn 5p orbitals in the SS, Ce_x-SS, and Pt_y/Ce_x-SS models. e) The computed PDOS diagrams of Sn-5p and O-2p orbital for NO_3^- adsorbed on SS, Ce_x-SS, and Pt_y/Ce_x-SS models. f) The calculated adsorption energies of NO_3^- and NO_2^- on SS, Ce_x-SS, and Pt_y/Ce_x-SS models. g) Gibbs free energy diagram of various intermediates generated during eNO_3RR pathways over SS, Ce_x-SS, and Pt_y/Ce_x-SS models. The insets are the structural models that represent the adsorption form of various intermediates on Pt_y/Ce_x-SS during eNO_3RR. The azure, mauve, red, blue, and white balls refer to S, Sn, O, N and H atoms.

and can facilitate the following conversion of NO_2^- to NH_3, which is consistent with the experimental results and plays a decisive role in the improvement of eNO_3RR (Figure 4e). To evaluate the HER performance on the catalysts, we also compute the adsorption energy of H_2O and Gibbs adsorption free energies of *H (Figure S33, Supporting Information). As a result, all the binding energies of H_2O are much weaker than that of NO_3^- and NO_2^- in each sample, ensuring the strong interaction of NO_3^- and NO_2^- for their further reduction. Also, no matter whether on Sn or S site, the calculated ΔG_{H^*} on Pt_y/Ce_x-SS is much higher than that on SS and Ce_x-SS, and all the ΔG_{H^*} are positive values, demonstrating the obstructive HER activity. Overall, assisted by the diatomic Pt-Ce pairs, the SS NS with compressed interlayer spacing leads to the delocalization of p-orbital electrons, and such delocalized electrons enhance the chemical affinity between catalytic sites and NO_3^- and NO_2^- reactants. Additionally, the compressed interlayer spacing increases the ΔG_{H^*} and thus inhibits the unwanted HER activity. Consequently, these are the origin of the remarkable performance of the $Pt_{0.9}/Ce_{0.5}$-SS for eNO_3RR. Finally, based on DFT calculation, we proposed possible reaction pathways and calculated the corresponding ΔG of each intermediate over Ce_x-SS, SS, and Pt_y/Ce_x-SS models (Figure 5g and Figures S34–S36, Supporting Information). Generally, the eNO_3RR process includes the adsorption of NO_3^-, deoxygenation, hydrogenation, and the desorption of NH_3. For the hydrogenation, we proposed two possible pathways, i.e., *NOH→*NHOH→*NH_2OH and *NOH→*N→*NH. As depicted in Figure 5g, the

© 2022 Wiley-VCH GmbH

16146840, 2023, 6, Downloaded from https://onlinelibrary.wiley.com/doi/10.1002/aenm.202203201 by City University Of Hong Kong, Wiley Online Library on [14/03/2023]. See the Terms and Conditions (https://onlinelibrary.wiley.com/terms-and-conditions) on Wiley Online Library for rules of use; OA articles are governed by the applicable Creative Commons License

downward trend from NO_3^- to $*NO_3$ suggests an energetically favorable reaction. However, in the following $*NO_3 \rightarrow *NO_2$, Pt_y/Ce_x-SS involve an uphill free energy increment (+0.09 eV), and those for SS and Ce_x-SS are +0.28 eV and +0.31 eV, respectively. These upward thermodynamic changes reveal this system's RDS. The stark contrast from Pt_y/Ce_x-SS to SS and Ce_x-SS indicates the promotion of RDS thermodynamically by the interlayer spacing regulation. Further, it theoretically gives the origin of the remarkable performance of $Pt_{0.9}/Ce_{0.5}$-SS. Moreover, the higher ΔG of Pt_y/Ce_x-SS for producing HNO_2 demonstrates the difficulty in desorbing $*NO_2$. Subsequently, due to the unfavorable hydrogen adsorption over the catalysts, the protonation of $*NO \rightarrow *NOH$ requires an energy uphill again. Overall, the higher $NO_3^- \rightarrow *NO_3$ but lower $*NO_2 \rightarrow NO_2^-$ energy change and the facilitated RDS ($*NO_3 \rightarrow *NO_2$) sufficiently illustrate that the interlayer spacing regulation strategy can effectively facilitate the conversion from NO_3^- to NH_3 for both activity and selectivity.

3. Conclusions

In summary, we demonstrate an interlayer spacing engineering on 2D SnS nanosheets by adopting active diatomic Pt-Ce pairs that significantly improve NO_3^--to-NH_3 conversion for both activity and selectivity. Specifically, the tailored interlayer spacing realizes a linear expansion and compression rate from 6.49% to 7.97% compared to the intrinsic value of SnS (5.672 ± 0.019 Å). Taking together the experimental results, in situ Raman spectra, and DFT calculation, it reveals that the interlayer spacing regulation can tune the electron density of localized p-orbital in Sn into its delocalized states, thus enhancing the chemical affinity towards NO_3^- and NO_2^- but inhibiting hydrogen evolution simultaneously and promoting the rate-determining step of $*NO_3 \rightarrow *NO_2$ in eNO_3RR. Consequently, the designed SnS catalysts show an excellent FE for NH_3 (94.12%) and Y_{NH3} (0.3056 mmol cm^{-2} h^{-1}) at –0.5 V versus RHE. By the strong chemical interaction between Ce and Pt atoms, this work provides a powerful strategy for tailoring flexible interlayer spacing of 2D materials, opening a new avenue for constructing high-performance catalysts for ammonia synthesis.

Supporting Information

Supporting Information is available from the Wiley Online Library or from the author.

Acknowledgements

This work was supported by the Environment and Conservation Fund of Hong Kong SAR, China (Grant No. ECF 2020-13), a fellowship award from the Research Grants Council of the Hong Kong SAR, China (CityU RFS2021-1S04), the Foshan Innovative and Entrepreneurial Research Team Program (Grant No. 2018IT100031), and the City University of Hong Kong (Project No. 9667227).

Conflict of Interest

The authors declare no conflict of interest.

Data Availability Statement

The data that support the findings of this study are available from the corresponding author upon reasonable request.

Keywords

diatomic Pt-Ce, chemical affinity, electrochemical nitrate reduction, interlayer spacing regulation, p-orbital delocalization

Received: September 21, 2022
Revised: November 15, 2022
Published online: December 13, 2022

[1] L. Ye, R. Nayak-Luke, R. Banares-Alcantara, E. Tsang, *Chem* **2017**, *3*, 712.
[2] V. Kyriakou, I. Garagounis, A. Vourros, E. Vasileiou, M. Stoukides, *Joule* **2020**, *4*, 142.
[3] H. Jin, L. Li, X. Liu, C. Tang, W. Xu, S. Chen, L. Song, Y. Zheng, S. Z. Qiao, *Adv. Mater.* **2019**, *31*, 1902709.
[4] X. Zhao, G. Hu, G. F. Chen, H. Zhang, S. Zhang, H. Wang, *Adv. Mater.* **2021**, *33*, 2007650.
[5] K. P. Ramaiyan, S. Ozden, S. Maurya, D. Kelly, S. K. Babu, A. Benavidez, F. G. Garzon, Y. S. Kim, C. R. Kreller, R. Mukundan, *J. Electrochem. Soc.* **2020**, *167*, 044506.
[6] Y. Guo, R. Zhang, S. Zhang, Y. Zhao, Q. Yang, Z. Huang, B. Dong, C. Zhi, *Energy Environ. Sci.* **2021**, *14*, 3938.
[7] R. Zhang, Y. Guo, S. Zhang, D. Chen, Y. Zhao, Z. Huang, L. Ma, P. Li, Q. Yang, G. Liang, *Adv. Energy Mater.* **2022**, *12*, 2103872.
[8] W. He, J. Zhang, S. Dieckhöfer, S. Varhade, A. C. Brix, A. Lielpetere, S. Seisel, J. R. Junqueira, W. Schuhmann, *Nat. Commun.* **2022**, *13*, 1.
[9] H. Liu, X. Lang, C. Zhu, J. Timoshenko, M. Rüscher, L. Bai, N. Guijarro, H. Yin, Y. Peng, J. Li, *Angew. Chem., Int. Ed.* **2022**, *61*, e202202556.
[10] G.-F. Chen, Y. Yuan, H. Jiang, S.-Y. Ren, L.-X. Ding, L. Ma, T. Wu, J. Lu, H. Wang, *Nat. Energy* **2020**, *5*, 605.
[11] M. Bajdich, M. García-Mota, A. Vojvodic, J. K. Nørskov, A. T. Bell, *J. Am. Chem. Soc.* **2013**, *135*, 13521.
[12] T. Hu, C. Wang, M. Wang, C. M. Li, C. Guo, *ACS Catal.* **2021**, *11*, 14417.
[13] A. Khorshidi, J. Violet, J. Hashemi, A. A. Peterson, *Nat. Catal.* **2018**, *1*, 263.
[14] Y. Zhang, F. Gao, H. You, Z. Li, B. Zou, Y. Du, *Coord. Chem. Rev.* **2022**, *450*, 214244.
[15] D. Schilter, *Nat. Rev. Chem.* **2018**, *2*, 1.
[16] W. Qian, S. Xu, X. Zhang, C. Li, W. Yang, C. R. Bowen, Y. Yang, *Nano-Micro Lett.* **2021**, *13*, 1.
[17] F. Gao, Y. Zhang, F. Ren, Y. Shiraishi, Y. Du, *Adv. Funct. Mater.* **2020**, *30*, 2000255.
[18] F. Gao, Y. Zhang, Z. Wu, H. You, Y. Du, *Coord. Chem. Rev.* **2021**, *436*, 213825.
[19] P. Thangasamy, S. Oh, S. Nam, I.-K. Oh, *Carbon* **2020**, *158*, 216.
[20] J. Liang, S. Ma, J. Li, Y. Wang, J. Wu, Q. Zhang, Z. Liu, Z. Yang, K. Qu, W. Cai, *J. Mater. Chem.* **2020**, *8*, 10426.
[21] N. Zhang, J. Shang, X. Deng, L. Cai, R. Long, Y. Xiong, Y. Chai, *ACS Nano* **2022**, *16*, 4795.
[22] Q. Fu, H. Saltsburg, M. Flytzani-Stephanopoulos, *Science* **2003**, *301*, 935.
[23] Y. Nagai, T. Hirabayashi, K. Dohmae, N. Takagi, T. Minami, H. Shinjoh, S. Matsumoto, *J. Catal.* **2006**, *242*, 103.
[24] M. Yoo, Y.-S. Yu, H. Ha, S. Lee, J.-S. Choi, S. Oh, E. Kang, H. Choi, H. An, K.-S. Lee, *Energy Environ. Sci.* **2020**, *13*, 1231.

© 2022 Wiley-VCH GmbH

16146840, 2023, 6, Downloaded from https://onlinelibrary.wiley.com/doi/10.1002/aenm.202203201 by City University Of Hong Kong, Wiley Online Library on [14/03/2023]. See the Terms and Conditions (https://onlinelibrary.wiley.com/terms-and-conditions) on Wiley Online Library for rules of use; OA articles are governed by the applicable Creative Commons License

[25] A. Beniya, S. Higashi, *Nat. Catal.* **2019**, *2*, 590.
[26] Y. Shi, Z. Li, J. Wang, R. Zhou, *Appl. Catal. B* **2021**, *286*, 119936.
[27] N. L. Hamidah, M. Shintani, A. S. Ahmad Fauzi, G. K. Putri, S. Kitamura, K. Hatakeyama, M. Sasaki, A. T. Quitain, T. Kida, *ACS Appl. Nano Mater.* **2020**, *3*, 4292.
[28] M. Chen, S. Wan, L. Zhong, D. Liu, H. Yang, C. Li, Z. Huang, C. Liu, J. Chen, H. Pan, *Angew. Chem., Int. Ed.* **2021**, *60*, 26233.
[29] X. Chia, P. Lazar, Z. k. Sofer, J. Luxa, M. Pumera, *J. Phys. Chem. C* **2016**, *120*, 24098.
[30] M. Li, Y. Wu, T. Li, Y. Chen, H. Ding, Y. Lin, N. Pan, X. Wang, *RSC Adv.* **2017**, *7*, 48759.
[31] K. Sato, K. Yamada, K. Sakowski, M. Iwaya, T. Takeuchi, S. Kamiyama, Y. Kangawa, P. Kempisty, S. Krukowski, J. Piechota, *Appl. Phys. Express* **2021**, *14*, 096503.
[32] Y. Jiang, D. Song, J. Wu, Z. Wang, S. H , Y. Xu, Z. Chen, B. Zhao, J. Zhang, *ACS Nano* **2019**, *13*, 9100.
[33] L. Wang, X. Zhang, Y. Xu, C. Li, W. Liu, S. Yi, K. Wang, X. Sun, Z. Wu, Y. Ma, *Adv. Funct. Mater.* **2021**, *31*, 2104286.
[34] Y. Ding, M. Zeng, Q. Zheng, J. Zhang, D. Xu, W. Chen, C. Wang, S. Chen, Y. Xie, Y. Ding, *Nat. Commun.* **2021**, *12*, 1.
[35] Z. Chen, K. Leng, X. Zhao, S. Malkhandi, W. Tang, B. Tian, L. Dong, L. Zheng, M. Lin, B. S. Yeo, *Nat. Commun.* **2017**, *8*, 1.
[36] Y. Bo, H. Wang, Y. Lin, T. Yang, R. Ye, Y. Li, C. Hu, P. Du, Y. Hu, Z. Liu, *Angew. Chem., Int. Ed.* **2021**, *60*, 16085.
[37] J. He, W. Li, P. Xu, J. Sun, *Appl. Catal. B* **2021**, *298*, 120528.
[38] N. Padma, *Handbook on Synthesis Strategies for Advanced Materials*, Springer, XX **2022**, pp. 377.
[39] P.-C. Huang, Y.-M. Shen, S. Brahma, M. O. Shaikh, J.-L. Huang, S.-C. Wang, *Catalysts* **2017**, *7*, 252.
[40] M. Liu, K. A. Min, B. Han, L. Y. S. Lee, *Adv. Energy Mater.* **2021**, *11*, 2101281.
[41] W. Xu, G. Fan, J. Chen, J. Li, L. Zhang, S. Zhu, X. Su, F. Cheng, J. Chen, *Angew. Chem., Int. Ed.* **2020**, *59*, 3511.
[42] S. Zhang, D. Chen, Z. Liu, M. Ruan, Z. Guo, *Appl. Catal. B* **2021**, *284*, 119686.
[43] P. Li, W. Fu, P. Zhuang, Y. Cao, C. Tang, A. B. Watson, P. Dong, J. Shen, M. Ye, *Small* **2019**, *15*, 1902535.
[44] L. Li, C. Tang, B. Xia, H. Jin, Y. Zheng, S.-Z. Qiao, *ACS Catal.* **2019**, *9*, 2902.
[45] X. Chen, Y.-T. Liu, C. Ma, J. Yu, B. Ding, *J. Mater. Chem.* **2019**, *7*, 22235.
[46] Z.-Y. Wu, M. Karamad, X. Yong, Q. Huang, D. A. Cullen, P. Zhu, C. Xia, Q. Xiao, M. Shakouri, F.-Y. Chen, *Nat. Commun.* **2021**, *12*, 1.
[47] M. X. Jin, Y. L. Pu, Z. J. Wang, Z. Zhang, L. Zhang, A. J. Wang, J. J. Feng, *ACS Appl. Energy Mater.* **2019**, *2*, 4188.
[48] M. Duca, M. T. Koper, *Energy Environ. Sci.* **2012**, *5*, 9726.
[49] S. Garcia-Segura, M. Lanzarini-Lopes, K. Hristovski, P. Westerhoff, *Appl. Catal. B* **2018**, *236*, 546.
[50] Y. Wang, A. Xu, Z. Wang, L. Huang, J. Li, F. Li, J. Wicks, M. Luo, D. H. Nam, C. S. Tan, Y. Ding, J. Wu, Y. Lum, C. T. Dinh, D. Sinton, G. Zheng, E. H. Sargent, *J. Am. Chem. Soc.* **2020**, *142*, 5702.
[51] K. Qi, X. Cui, L. Gu, S. Yu, X. Fan, M. Luo, S. Xu, N. Li, L. Zheng, Q. Zhang, *Nat. Commun.* **2019**, *10*, 1.
[52] Y. Zheng, T. Deng, N. Yue, W. Zhang, X. Zhu, H. Yang, X. Chu, W. Zheng, *J Raman Spectrosc* **2021**, *52*, 2119.
[53] D. Philip, A. Eapen, G. Aruldhas, *J. Solid State Chem.* **1995**, *116*, 217.
[54] M. Asadi, B. Kumar, A. Behranginia, B. A. Rosen, A. Baskin, N. Repnin, D. Pisasale, P. Phillips, W. Zhu, R. Haasch, *Nat. Commun.* **2014**, *5*, 4470.
[55] S. Sun, X. Zhou, B. Cong, W. Hong, G. Chen, *ACS Catal.* **2020**, *10*, 9086.
[56] Z. Chen, Y. Song, J. Cai, X. Zheng, D. Han, Y. Wu, Y. Zang, S. Niu, Y. Liu, J. Zhu, *Angew. Chem., Int. Ed.* **2018**, *130*, 5170.
[57] S. He, F. Ni, Y. Ji, L. Wang, Y. Wen, H. Bai, G. Liu, Y. Zhang, Y. Li, B. Zhang, *Angew. Chem., Int. Ed.* **2018**, *130*, 16346.
[58] H. Shin, Y. Ha, H. Kim, *J. Phys. Chem. Lett.* **2016**, *7*, 4124.

© 2022 Wiley-VCH GmbH

16146840, 2023, 6, Downloaded from https://onlinelibrary.wiley.com/doi/10.1002/aenm.202203201 by City University Of Hong Kong, Wiley Online Library on [14/03/2023]. See the Terms and Conditions (https://onlinelibrary.wiley.com/terms-and-conditions) on Wiley Online Library for rules of use; OA articles are governed by the applicable Creative Commons License